PAPER

Check for updates

Reactive CO_2 capture and mineralization of magnesium hydroxide to produce hydromagnesite with inherent solvent regeneration†

Xun Gao,[a] Peilong Lu,[a] Ivan Kuzmenko,[b]
Jan Ilavsky (iD) [b] and Greeshma Gadikota (iD) *[ac]

Valorization of multiple low value streams including CO_2 emissions and magnesium-hydroxide bearing mine tailings to produce magnesium carbonate through reactive CO_2 capture and mineralization provides a less explored opportunity to manage several gigatons of CO_2 emissions. To resolve the feasibility of converting magnesium hydroxide to magnesium carbonate through reactive CO_2 capture and mineralization, CO_2 capture solvents such as sodium glycinate are harnessed to capture CO_2 and react directly with $Mg(OH)_2$ to produce hydromagnesite ($Mg_5[(CO_3)_4(OH)_2] \cdot 4H_2O$). This approach eliminates the energy-intensive step of producing high purity CO_2 associated with regenerating the solvent, and redissolving CO_2 to produce magnesium carbonate. Interestingly, while temperatures below 50 °C facilitate CO_2 capture, the mineralization kinetics are slow. However, at higher temperatures, accelerated carbon mineralization is favored by the faster kinetics of $Mg(OH)_2$ dissolution and precipitation of magnesium carbonate. Reacting $Mg(OH)_2$ at 90 °C with 15 wt% solids in the presence of 2.5 M sodium glycinate after 3 hours under well-stirred conditions results in an extent of carbon mineralization of 75.5%. The theoretical maximum extent of carbon mineralization when hydromagnesite is formed is 80%. Pre-loading CO_2 on the solvent is also an effective approach to ensure that sufficient CO_2 is available for reactive CO_2 capture and mineralization, particularly when dilute CO_2 and N_2 mixtures are used. Higher extents of carbon mineralization are associated with an increase in the particle size and a reduction in the cumulative pore volume. These insights unlock the feasibility of harnessing reactive CO_2 capture and mineralization as a pathway to convert magnesium-hydroxide bearing resources into industrially relevant magnesium carbonate products.

Keywords: Reactive CO_2 capture and mineralization; Magnesium hydroxide; Magnesium carbonate; Regenerable CO_2 capture solvents; Hydromagnesite.

1 Introduction

Harnessing multiple emissions such as CO_2-bearing flue gas streams and magnesium hydroxide (or brucite) bearing tailings is emerging as a viable approach to capture and store CO_2 emissions as stable magnesium carbonates, given the thermodynamically downhill nature of carbon mineralization pathways.[1,2] The direct carbon mineralization of $Mg(OH)_2$-bearing mine tailings with CO_2 in ultra-dilute streams

including air and flue gas is feasible but kinetically slow.[1,3] Alternatively, bubbling highly concentrated or nearly pure CO_2 through $Mg(OH)_2$ is known to facilitate rapid carbon mineralization within two hours or less.[4] However, CO_2 capture technologies are needed to concentrate CO_2 that can be used for subsequent carbon mineralization using this approach.[5,6] To achieve fast kinetics of carbon mineralization while directly harnessing ultra-dilute sources of CO_2 including flue gas streams or even air without additional steps to regenerate the solvents and solubilize CO_2, reactive CO_2 capture and mineralization pathways are being developed.[7]

Reactive CO_2 capture and mineralization pathways involve concentrating CO_2 emissions to produce CO_2 – loaded solvents. These CO_2 – loaded solvents react directly with the alkaline source to produce the respective carbonates with concurrent regeneration.[8] This approach is designed to circumvent: (i) the low solubility of CO_2 by harnessing CO_2

[a] *School of Civil and Environmental Engineering, Cornell University, Ithaca, NY 14853, USA. E-mail: gg464@cornell.edu; Tel: +1 607 255 4796*
[b] *Advanced Photon Source, Argonne National Laboratory, Lemont, IL 60439, USA*
[c] *Smith School of Chemical and Biological Engineering, Cornell University, Ithaca, NY 14853, USA*

† Electronic supplementary information (ESI) available. See DOI: https://doi.org/10.1039/d4im00157e

capture solvents with basic functionalities that enhance CO_2 solubility at very low gas phase concentrations, (ii) energy needs associated with producing high purity CO_2 for subsequent mineralization, and (iii) the additional unit operations associated with producing high purity CO_2 which occurs conventionally *via* pressure – swing or thermal – swing sorption processes.

The efficacy of these pathways for mineralizing calcium – bearing resources, such as oxides and silicates, and heterogeneous resources, such as fly ash, has been verified by harnessing polyamines and water-lean solvents such as 1,8-diazabicyclo[5.4.0]undec-7-ene (DBU), branched amines such as 2-amino-2-methyl-1-propanol (AMP), monoamines such as monoethanolamine (MEA), and amino acid salts with varying alkyl functional groups such as sodium glycinate and sodium sarcosinate.[9–14] These studies established that temperatures in range of 50–75 °C facilitate reactive CO_2 capture and mineralization, with lower temperatures favouring CO_2 capture but challenged by slow mineralization kinetics, whereas higher temperatures enable faster carbon mineralization but limit CO_2 capture.

While the efficacy of reactive CO_2 capture and mineralization of magnesium oxide was established using amine bearing solvents, the use of more environmentally benign solvents such as sodium glycinate has not been explored.[15] Sodium glycinate is the simplest unit of amino acid salts. Establishing the efficacy of reactive CO_2 capture and mineralization using this amino acid salt translates into the use of other amino acids with multiple amine groups, straight and branched alkyl groups, and varying positions of amine groups (*e.g.*, alpha and beta positions) for this approach. Regardless of the placement of the amine functional groups, the key reactions associated with reactive CO_2 capture and mineralization include: (i) CO_2 hydration, (ii) dissolution of $Mg(OH)_2$, and (iii) the formation of Mg-carbonate, which is shown in Fig. 1.[16]

Despite considerable advances made in reactive CO_2 capture and mineralization,[15] several outstanding research questions remain including: (i) is reactive CO_2 capture and mineralization of $Mg(OH)_2$ favoured at temperatures above or below 50 °C and why? (ii) How does the reactivity of $Mg(OH)_2$ compare with that of Ca-bearing oxides and silicates for reactive CO_2 capture and mineralization at comparable experimental conditions? (iii) Given that Mg^{2+} ions have a stronger hydration shell compared to Ca^{2+} ions,[17] what is the influence of reactive CO_2 capture and mineralization on the structural evolution of magnesium carbonate phases? For example, are metastable hydrated magnesium carbonate phases formed as opposed to stable magnesite forms? (iv) What is the influence of CO_2 compositions in the range of 4–20 vol% on reactive CO_2 capture and mineralization of $Mg(OH)_2$? (v) What is the influence of the extent of carbon mineralization on the pore and particle morphological evolution of the Mg-bearing materials?

To address these questions, reactive CO_2 capture and mineralization studies are conducted with 1 M and 2.5 M Na-glycinate contrasted with water at temperatures in the range of 25–90 °C with CO_2 concentrations ranging from 4–100 vol%. The morphological features of the materials are characterized before and after carbon mineralization to determine the influence of carbon mineralization on the particle and pore morphologies of the products.

2 Results and discussion

### 2.1 Reactive CO_2 capture and mineralization of magnesium hydroxide

Reactive CO_2 capture and mineralization involves harnessing CO_2 capture solvents to capture and concentrate CO_2 in the aqueous phase and reacting these CO_2-loaded solvents with an alkaline source to produce Mg-carbonate and regenerate the solvent. In this multiphase chemical reaction pathway, the solubility of CO_2, reactivity of the alkaline source, and subsequent carbon mineralization behaviour are influenced by temperature, solvent concentration, and pH of the system. CO_2 capture is aided at temperatures below 40 °C while mineralization kinetics are aided at higher temperatures. Furthermore, the solubility of magnesium carbonates decreases with temperature, thus favouring precipitation. To resolve the influence of temperature, reactive CO_2 capture and mineralization behaviour with $Mg(OH)_2$ is investigated at 25, 50, 75, and 90 °C. The reactivity of $Mg(OH)_2$ is established with water, 1.0 M and 2.5 M sodium glycinate. Furthermore, the reactivity of $Mg(OH)_2$ is compared with that of calcium oxide and calcium silicate at comparable experimental conditions to contrast their reactivity. These results are discussed in this section.

To investigate the influence of temperature, experiments are conducted in a pure CO_2 environment with 1.0 M and 2.5 M Na-glycinate and deionized water for comparison at 25, 50, 75, and 90 °C, respectively. As shown in Fig. 2, the extent of carbon mineralization increases from 17.1% at 25 °C to 75.5% at 90 °C when $Mg(OH)_2$ is reacted in the presence of 2.5 M Na-glycinate. This enhancement in carbon mineralization which is more than three-fold indicates that the fast kinetics of carbon mineralization and lower solubility of Mg-carbonate at higher temperature of 90 °C dominate
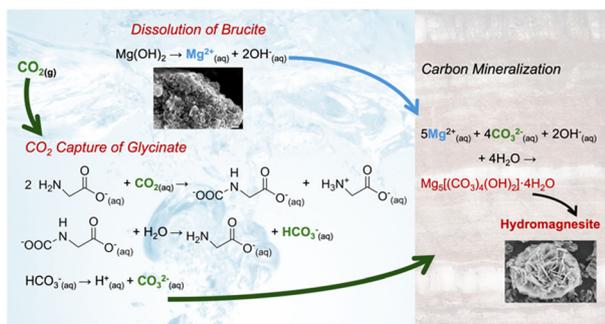
Fig. 1 Schematic representation of reactive CO_2 capture and carbon mineralization by harnessing $Mg(OH)_2$ as the alkaline source and Na-glycinate as the CO_2 capture solvent.
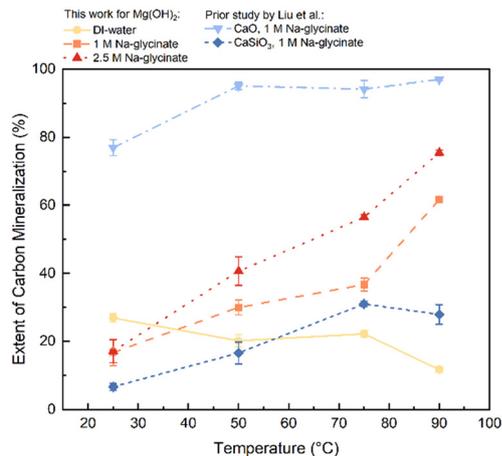
Fig. 2 The extents of carbon mineralization of $Mg(OH)_2$ with various Na-glycinate concentrations at different temperatures. All experiments are conducted at 1 atm of CO_2. The solid products were analyzed by thermogravimetric analysis (TGA). Extents of carbon mineralization reported for CaO and $CaSiO_3$ from Liu and coworkers are included for comparison.[18]

higher solubility of CO_2 at lower temperatures.[19–21] In the absence of the solvent, extents of carbon mineralization decreased from 26.9% at 25 °C to 22.2% at 75 °C and to 11.7% at 90 °C, respectively, due to the reduced solubility of CO_2 with rising temperature which limits the availability of carbonate species needed for carbon mineralization.[22] In contrast, calcium oxide is highly reactive, and carbon mineralization extents of 80% or higher are achieved at 25 °C or above. Interestingly, the reactivity of $CaSiO_3$ increases to 31% at 75 °C and decreases at 90 °C. These results show that Ca-bearing solids are more reactive at temperatures below 90 °C. The significantly lower extents of carbon mineralization noted using Ca–silicate are attributed to the slow dissolution rate of silicate materials and the formation of silica passivation layer that may limit the diffusivity of the ions for carbon mineralization.[23–25]

Investigations of the influence of 1 M and 2.5 M Na-glycinate on reactive CO_2 capture and mineralization showed that higher extents of carbon mineralization are achieved with 2.5 M Na-glycinate compared to 1 M counterparts due to the greater availability of amine functional groups for reactive CO_2 capture and mineralization. Specifically, extents of carbon mineralization achieved with $Mg(OH)_2$ are 61.7% and 75.5% with 1 M and 2.5 M Na-glycinate, respectively, at 90 °C. It is important to note that the theoretical maximum extent of carbon mineralization for hydromagnesite is 80%, because the stoichiometric ratio of $Mg(OH)_2$ to CO_2 is determined to be 5:4 based on reaction 2. Assuming all $Mg(OH)_2$ reacts with CO_2, the EoC is calculated to be 80% based on eqn (3) and (4). As a result, the normalized extent of carbon mineralization is up to 94.3% for the 2.5 M Na-glycinate case at 90 °C (Fig. S1†). It is also worth noting that the extents of carbon mineralization of $Mg(OH)_2$ at 25 °C in the presence of water, 1 M and 2.5 M Na-glycinate are 26.9%,

16.7%, and 17.1%, respectively. At 25 °C, the glycinate ligands can bind with the Mg^{2+} ions in the slurry to form Mg–glycinate complexes, which may be too stable to react with (bi)carbonate species to produce Mg-carbonates.[26]

While the efficacy of harnessing highly concentrated CO_2 streams for the reactive CO_2 capture and mineralization of $Mg(OH)_2$ to produce the respective Mg-carbonate has been established, the influence of the dilute CO_2 streams or flue gas which are representative of industrial operations remains less studied. Flue gas is the tail gas bearing nitrogen, carbon dioxide, and steam with trace amount of sulfur oxide or nitrogen oxide emerging from fuel combustion, industrial calcination or reduction processes.[27,28] To simulate the conditions of industrial flue gases, a binary gas mixture of nitrogen and carbon dioxide is prepared and used to investigate reactive CO_2 capture and mineralization with magnesium hydroxide.

As shown in the experimental section reactive CO_2 capture and mineralization studies are conducted with binary mixture of N_2 and CO_2 inside a gas circulation system with CO_2-preloaded solutions at 25 °C. A constant binary gas flow is injected into the $Mg(OH)_2$ slurry as the CO_2 source. Following the same calculation approach, the carbon mineralization extents from flue gas having varying CO_2 levels with different pre-loading protocols are shown in Fig. 3. Generally, as the CO_2 concentration in the binary gas flow increases from 4% to 20%, the extent of carbon mineralization increases from 3.4% to 31% in cases without CO_2 pre-loading. The monotonically increasing correlation is aligned with Henry's law, by which CO_2 solubility and dissolution rate are determined by the CO_2 partial pressure, equivalent to the CO_2 concentration in the flue gas.[29] This observation indicates that increasing CO_2 concentrations can linearly improve the extent of carbon mineralization by enhancing the amount of dissolved CO_2. In contrast, CO_2 pre-loading remarkably increases the extent of carbon mineralization compared to the cases without CO_2 pre-loading, with increases of 15.2%, 19.9%, 26.8%, and 33.8%
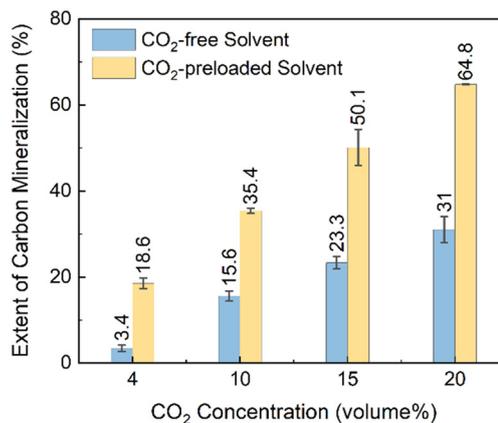
Fig. 3 The extents of carbon mineralization of $Mg(OH)_2$ using binary flue gas with various CO_2/N_2 ratios. The carbonate content in the solid products is analyzed by thermogravimetric analysis (TGA).

for 4, 10, 15, and 20 vol% CO_2 at 25 °C, with associated extents of 18.6%, 35.4%, 50.1%, and 64.8%, respectively.

The significant increase in the extents of carbon mineralization with pre-loaded solvents are attributed to the ready availability of dissolved carbon for reacting with $Mg(OH)_2$ to produce Mg-carbonate bearing species. This approach overcomes the challenge of the mass transfer of CO_2 from the gas to the liquid phase. Pre-loading the solvent with CO_2 also ensures that glycinate is effectively bound to CO_2 as opposed to Mg^{2+} ions to produce Mg-glycinate complexes. When Na-glycinate is mixed with $Mg(OH)_2$ before

Fig. 4 Evidence of (bi) carbonate species as determined using attenuated total reflection-Fourier transform infrared (ATR-FTIR) spectra for carbonate – bearing solid products obtained on reacting in (a) DI water, (b) 1 M Na-glycinate, and (c) 2.5 M Na-glycinate solutions. The characteristic peaks in the dotted square areas indicate the formation of HCO_3^- and CO_3^{2-} species.
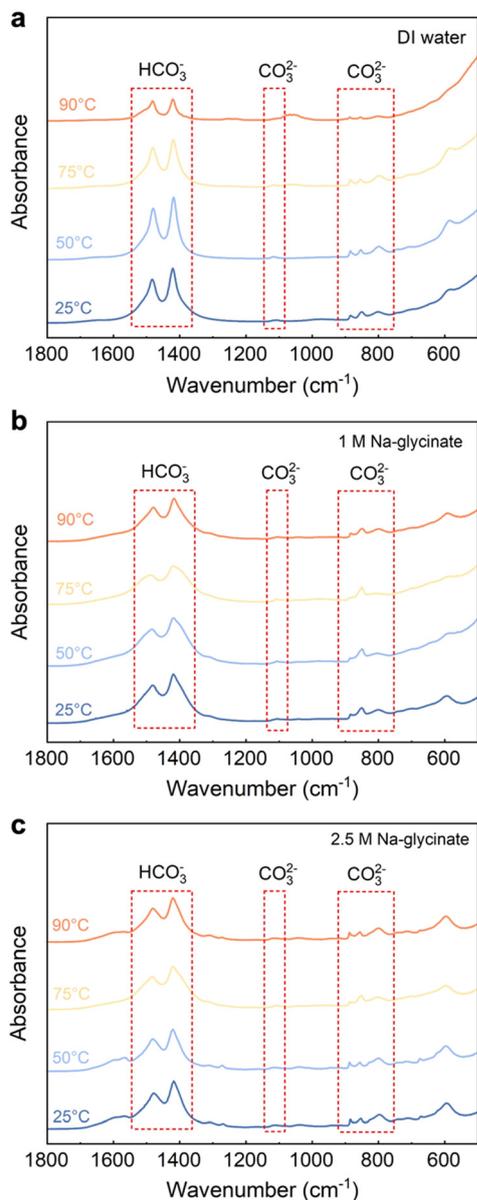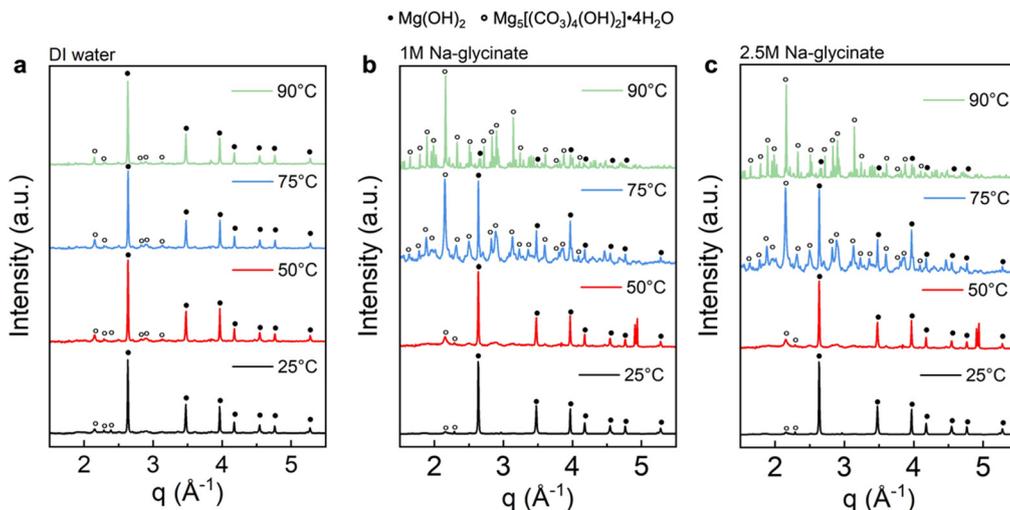
CO_2 is introduced, the formation of Mg-glycinate complex over CO_2-loaded Na-glycinate may limit CO_2 loading and subsequent reactivity with Mg^{2+} ions to produce hydromagnesite.

It is interesting to note that the extents of carbon mineralization are 61.7% and 75.5% with 100 vol% CO_2 without pre-loading 1.0 M and 2.5 M Na-glycinate solvent at 90 °C for a reaction time of 3 hours, respectively. In contrast, the extent of carbon mineralization is 64.4% with the pre-loaded 2.5 M Na-glycinate CO_2 capture solvent when reacted at 25 °C for 3 hours. These results demonstrate that pre-loading the CO_2 capture solvent is effective in enabling carbon mineralization at room temperature. Thus, these results show the feasibility of reactive CO_2 capture and mineralization with $Mg(OH)_2$ at 25 °C by harnessing pre-loaded CO_2 capture solvents.

2.2 Chemical and structural evolution during reactive CO_2 capture and mineralization

Evidence of carbonate formation in Mg-carbonate bearing products is established using attenuated total reflection Fourier transform-infrared (ATR FT-IR) spectroscopy and wide-angle X-ray scattering (WAXS). First, the formation of CO_3^{2-} symmetric stretching vibration at 1119 cm^{-1} in the products as determined using ATR FT-IR measurements confirms solid carbonate formation (Fig. 4).[30] The corresponding bending vibration of CO_3^{2-} is also detected at 885 cm^{-1}, 854 cm^{-1}, and 798 cm^{-1}, respectively.[31] Besides, the CO_3^{2-} asymmetric stretching vibration splits into two peaks at 1485 cm^{-1} and 1421 cm^{-1}, respectively, which emerges in all the carbonate-bearing products, indicating the existence of bicarbonate in the carbonate-bearing solids.[32] The identified infrared bands of different carbonate-bearing species and the corresponding assignments are listed in Table 1. The formation of hydromagnesite in the products is further confirmed through the wide-angle X-ray scattering (WAXS) measurements.

As shown in Fig. 5(a), the emerging peaks noted with black circles are observed after $Mg(OH)_2$ mineralization in DI water. These well-defined characteristic peaks correspond to hydromagnesite (PDF 98-001-1519, noted with open circle). Products obtained after reacting in water do not have prominent hydromagnesite peaks compared to brucite (PDF 98-000-0130, noted with closed circle), indicating low extents

Table 1 The infrared bands of various carbonate – bearing species and the corresponding assignments

Species	Band position (cm^{-1})	Assignment
CO_3^{2-}	1119	Symmetric stretching
CO_3^{2-}	885	Bending
	854	
	798	
HCO_3^-	1485	Asymmetric stretching
	1421	

© 2025 The Author(s). Co-published by the Institute of Process Engineering, Chinese Academy of Sciences and the Royal Society of Chemistry

Ind. Chem. Mater., 2025, **3**, 732–743 | **735**

• $Mg(OH)_2$ ○ $Mg_5[(CO_3)_4(OH)_2] \cdot 4H_2O$

Fig. 5 Evidence of hydromagnesite formation as determined using wide angle X-ray scattering (WAXS) patterns for the carbonate-bearing solid products obtained using (a) DI water, (b) 1 M Na-glycinate, and (c) 2.5 M Na-glycinate at different temperatures. Two types of crystal structures are observed: $Mg(OH)_2$, originating from unreacted brucite, and $Mg_5[(CO_3)_4(OH)_2] \cdot 4H_2O$, originating from the carbonate products.

of carbon mineralization. Additionally, the peak intensity of hydromagnesite showed negligible changes with temperature, demonstrating that carbon mineralization in DI water is not significantly influenced by temperature, which is consistent with the extents of carbon mineralization in Table 2.[33,34]

In sharp contrast, the presence of Na-glycinate solution, particularly at elevated temperature, resulted in products with more prominent characteristic peaks of hydromagnesite with higher intensity. As shown in Fig. 5(b) and (c), magnesium hydroxide is the dominant phase at 25 °C, while hydromagnesite formation increases with temperature. At 90 °C, the dominance of hydromagnesite phase over $Mg(OH)_2$ is noted.[34] Prominent peaks corresponding to hydromagnesite emerge at 75 °C with 2.5 M Na-glycinate and at 90 °C with 1.0 M Na-glycinate. Furthermore, WAXS results in Fig. 5 confirm the formation of hydromagnesite, as the only Mg-carbonate bearing phase formed. Hydromagnesite formation is known to be dominant at 25–90 °C and in alkaline environments.[35,36]

2.3. Morphological changes during reactive CO_2 capture and mineralization

Insights into the influence of carbon mineralization on the morphological evolution of Mg-carbonate are unlocked through particle and pore size analyses and microscopy, as discussed in the following sections.

2.3.1 Evolution in particle morphology on reactive CO_2 capture and mineralization. The morphological changes in the product during the mineralization are revealed by scanning electron microscopy (SEM) images. The unreacted particles are present as hexagonal flakes with diameters of several microns, which is typical for brucite given its hexagonal crystal structure (Fig. 6(a)).[37] On carbon mineralization, the hexagonal flakes transformed into nest-like hydromagnesite particles (Fig. 6(b)), which is a typical particle shape of hydromagnesite at pH range of 8–9 with an average particle size in the range of 10–15 μm.[36,38] As the temperature is increased to 90 °C, the hydromagnesite

Table 2 Summary of experimental conditions, corresponding extents of carbon mineralization (EoC), mean particle sizes, and pore volumes of the unreacted and reacted $Mg(OH)_2$ materials

	Temperature (°C)	EoC (%)	Mean particle size (μm)	Pore volume (cc g⁻¹)
$Mg(OH)_2$	—	—	7.85	0.047
H_2O	25	26.90 ± 1.28	15.41	0.133
	50	20.14 ± 1.88	16.97	0.218
	75	22.18 ± 0.93	19.85	0.118
	90	11.68 ± 0.85	15.63	0.101
1 M Na-glycinate	25	16.71 ± 3.88	7.77	0.066
	50	29.97 ± 2.17	9.64	0.071
	75	36.71 ± 1.93	16.75	0.036
	90	61.69 ± 0.35	18.43	0.026
2.5 M Na-glycinate	25	17.08 ± 3.38	8.17	0.016
	50	40.67 ± 4.25	9.63	0.02
	75	56.45 ± 0.72	20.56	0.011
	90	75.46 ± 0.77	19.30	0.008

particles became larger and more compact (Fig. 6(c)). Additionally, some of the nest-like particles transformed into flat lamellar particles due to a pH variation from 9.04 at 75 °C to 9.19 at 90 °C, which is consistent with previous studies.[36,39] As shown in Fig. 6(d) and (e), carbon mineralization with 2.5 M Na-glycinate solution generated more lamellar-shaped particles and possessed a more compact structure compared to counterparts with 1 M Na-glycinate solution, which can be attributed to higher pH values resulting from higher Na-glycinate concentrations (9.57 at 75 °C and 9.60 at 90 °C).[36]

2.3.2 Evolution of particle size distributions on reactive CO$_2$ capture and mineralization. The mechanisms of brucite dissolution and hydromagnesite precipitation are evident from the particle size distributions of the unreacted and reacted particles, as shown in Fig. 7. Unreacted brucite particles with sizes smaller than 10 μm dissolve preferentially particularly at 75 °C and 90 °C in the presence of water, 1 M and 2.5 M Na-glycinate and precipitate hydromagnesite. Increasing temperatures from 25 °C to 90 °C corresponds to higher extents of carbon mineralization (Fig. 2) and larger particle sizes (Fig. 7). Carbon mineralization in the presence of Na-glycinate *versus* water results in the growth of larger particles, particularly at elevated temperatures of 75 °C and 90 °C (Fig. 7). The mean particle diameters increased nearly 2.4 times from 7.85 μm to 19.3 μm on carbon mineralization. The dissolution of unreacted Mg(OH)$_2$ particles smaller than 10 μm and the subsequent growth of carbonate-bearing particles (~20 μm) with more distinct particle size distributions is evident in the presence of 1 M and 2.5 M Na-glycinate solutions at 90 °C, indicating the emergence of more distinct morphologies on carbon mineralization.

2.3.3 Evolution of pore size distributions on reactive CO$_2$ capture and mineralization. During carbon mineralization, dissolution is known to increase the pore volume while extensive carbonate growth reduces the pore volume. To delineate the competing effects of dissolution and carbonate growth, the pore volume distributions are determined using BET N$_2$ adsorption–desorption isotherms conducted at 77 K. The cumulative pore volume distributions demonstrate that the cumulative pore volume of the products increase when Mg(OH)$_2$ is reacted in water (Fig. 8(a)). Compared to the unreacted magnesium hydroxide, the significantly higher cumulative pore volume in the products obtained on reaction in water (as seen in Table 2) corresponds to low extents of carbon mineralization ranging from 11.7% to 26.9% within the temperature range of 25–90 °C and the dominance of dissolution over carbon mineralization. Interestingly, products obtained on reacting Mg(OH)$_2$ in 1.0 M Na-glycinate showed a higher cumulative pore volume at 25 °C and 50 °C with corresponding extents of reaction of 16.7% and 30%, respectively. In contrast, the cumulative pore volume decreased compared to the base case at 75 °C and 90 °C with the corresponding respective extents of carbon mineralization of 36.7% and 61.7%. The crossover in the cumulative pore volumes occurs between 50 °C and 75 °C with increasing extents of carbon mineralization. In addition to extensive carbonate growth
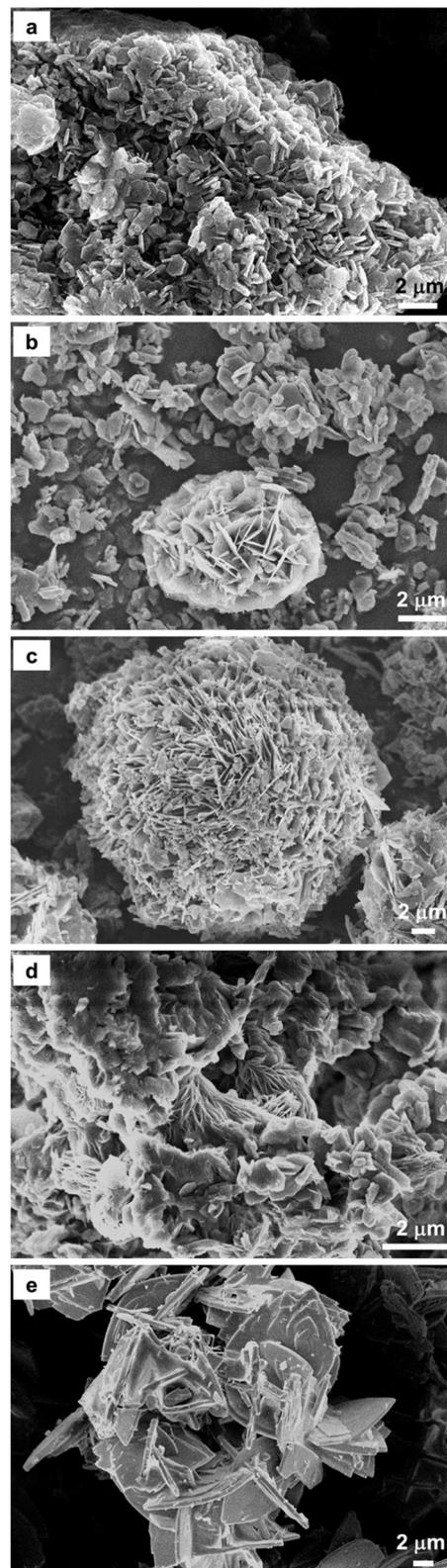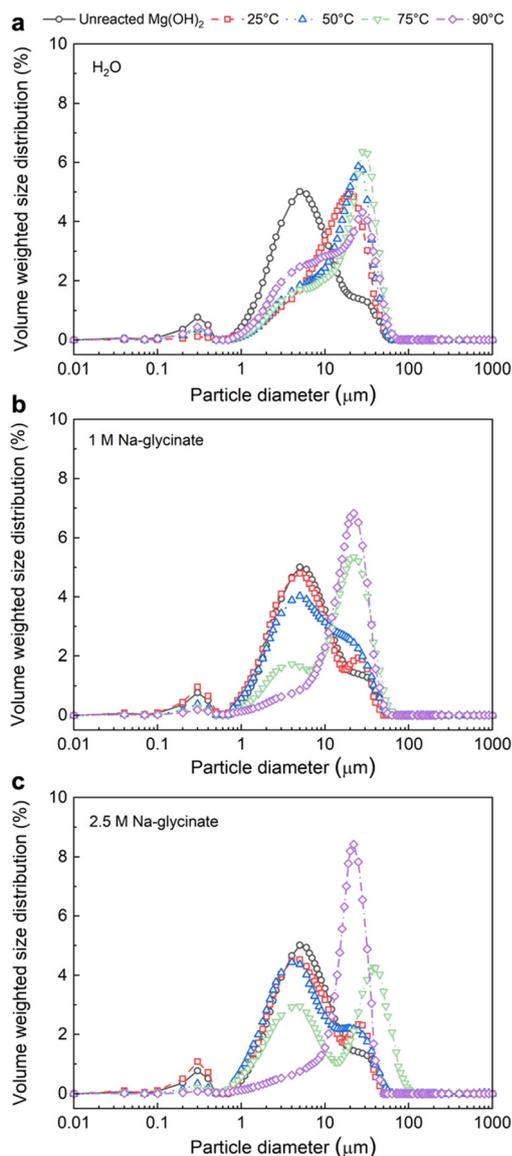

Fig. 6 Morphologies of (a) unreacted brucite, and carbonated solid with 1 M Na-glycinate solution at (b) 50 °C and (c) at 90 °C, and carbonated solid with 2.5 M Na-glycinate solution at (d) 50 °C and (e) 90 °C, determined by scanning electron micrographs (SEM).
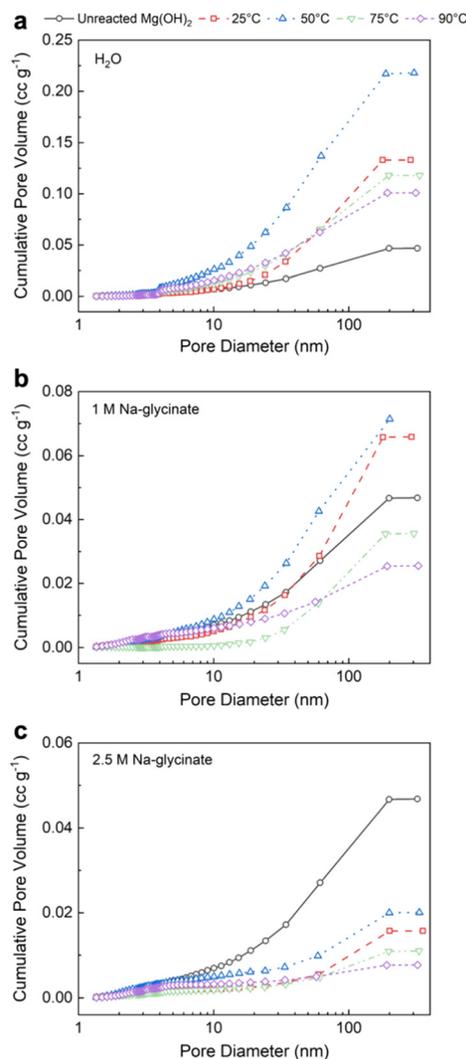
Fig. 7 Particle size distributions of the carbonate – bearing solids obtained with (a) DI water, (b) 1 M Na-glycinate solution, and (c) 2.5 M Na-glycinate solution. The size distributions are measured by light scattering instrument (PSA) with volume – based normalization of the particle size distributions.

Fig. 8 The cumulative pore volumes of various carbonate – bearing solids obtained using (a) DI water, (b) 1 M Na-glycinate solution, and (c) 2.5 M Na-glycinate solution. The pore volume distributions are determined using the Barrett, Joyner, Halenda (BJH) method with N_2 adsorption data.

decreasing the cumulative pore volume, nest-like hydromagnesite particles transform into denser lamellar morphologies with increasing alkalinity and at higher temperatures also decreases the cumulative pore volume compared to the unreacted material.[36,40]

It is interesting to note that with increasing temperature in the presence of higher concentration of 2.5 M Na-glycinate results in a lower cumulative pore volume at all temperatures of interest (Fig. 8(c)). The extensive formation of lamellar hydromagnesite (Fig. 6(d) and (e)) at higher temperatures in the presence of 2.5 M Na-glycinate corresponds to a 77% and 83% reduction in the pore volume at 75 °C and 90 °C, respectively (Table 2). Additionally, it is also worth noting

that the highest pore volume and specific surface area are observed at 50 °C for all cases, indicating that hydromagnesite formation is not as extensive at these conditions to close the pore spaces (Fig. S3†). The increase in the pore volume at 50 °C facilitates greater diffusion of ions or mass transfer enabling carbon mineralization.

These studies show that hydromagnesite with varying morphologies can be produced by tuning the temperatures associated with reactive CO_2 capture and mineralization with regenerable solvents such as Na-glycinate. Nest-like hydromagnesite at lower temperature is effective for flame retardant materials, while hydromagnesite with elongated lamellar particles can provide extra mechanical reinforcement as additives.[41,42]

Therefore, achieving tunable controls on the morphologies of the magnesium-carbonate bearing products unlocks new

opportunities for introducing these products produced by harnessing CO_2 emissions into markets for sustainable materials.

2.3.4 Mechanisms informed by chemo-morphological transformations. Mechanistic insights into reactive CO_2 capture and mineralization are established by probing and linking the coupled chemo-morphological transformations to the reactivity for producing solid magnesium carbonates (Table 2). When carbon mineralization of $Mg(OH)_2$ occurs in the presence of water without any carbon capture solvent, the relatively low extents of carbon mineralization below 27% and the significant increase in pore volume correspond to the dominance of $Mg(OH)_2$ dissolution over carbonate formation (Fig. 2 and Table 2).[36,43] In the presence of water alone, lower CO_2 solubility with rising temperature results in an inverse trend in decreasing extents of carbon mineralization with temperature. Limited CO_2 availability and associated proton availability limit the dissolution of $Mg(OH)_2$ and subsequent carbon mineralization.

In contrast, Na-glycinate enhances the solubility of CO_2 and provides sufficient concentration of (bi)carbonate species needed for carbon mineralization. While CO_2 capture is aided at lower temperatures of 25 °C and 50 °C, the kinetics of $Mg(OH)_2$ dissolution and the formation and precipitation of Mg-carbonate are aided at higher temperatures of 75 °C and 90 °C.[19,44] Therefore, higher extents of carbon mineralization of $Mg(OH)_2$ are noted at 75 °C and 90 °C relative to 25 °C and 50 °C. Interestingly, pre-loading the solvent with CO_2 prior to reactive CO_2 capture and mineralization overcomes the limitation of CO_2 mass transfer from the gas to the liquid phase and provides a ready supply of carbonate species which enables rapid carbon mineralization as noted in Fig. 3. Higher concentrations of Na-glycinate of 2.5 M provide additional functional groups and enhanced alkalinity to enhance CO_2 capture and mineralization compared to the 1 M Na-glycinate case (Fig. 2 and Table 2). The formation of hydromagnesite as the preferential magnesium carbonate phase is consistent with alkalinity, temperature, and ionic environments.[45]

Elevated temperature of 75 °C and 90 °C and enhanced alkalinity in the case of 2.5 M Na-glycinate facilitates the preferential formation of lamellar-shaped over nest-like hydromagnesite (Fig. 6). Carbon mineralization proceeds *via* the dissolution of particles smaller than 20 μm and the precipitation of Mg-carbonate particles with larger particle sizes (Fig. 7). The evolution of well-defined particle size distributions on extensive carbon mineralization is consistent with prior studies indicating that extensive carbonate formation in olivine ((Mg, $Fe)_2SiO_4$) results in distinct particle size distributions.[46,47] The extensive formation of hydromagnesite phases and extents of carbon mineralization exceeding 60% are associated with >77% decrease in the cumulative pore volume (Fig. 8). These analyses establish the chemo-morphological mechanisms underlying reactive CO_2 capture and mineralization using $Mg(OH)_2$. These studies complement prior studies that discuss the feasibility of reactive CO_2 capture and mineralization pathways by harnessing Ca – bearing alkaline sources.[8–10,18,48–50]

3 Conclusions

Reactive CO_2 capture and mineralization of $Mg(OH)_2$ to produce hydromagnesite ($Mg_5[(CO_3)_4(OH)_2]\cdot4H_2O$) by harnessing CO_2 capture solvents such as Na-glycinate is established at concentrations of 1.0 M and 2.5 M and temperatures ranging from 25 to 90 °C. Reacting $Mg(OH)_2$ at 90 °C with 15 wt% solids in the presence of 2.5 M sodium glycinate after 3 hours under well-stirred conditions results in an extent of carbon mineralization of 75.5%. In contrast, the extents of carbon mineralization in the presence of water without any solvent do not exceed 27% at all conditions of temperature. As a reference, the maximum possible extent of carbon mineralization is 80% when 100% hydromagnesite is produced. The coupled effects of enhanced kinetics of magnesium hydroxide dissolution and Mg-carbonate precipitation at elevated temperatures of 75 °C and 90 °C dominate favourable CO_2 uptake by solvents at lower temperature of 25 °C. Well-defined particle size distributions and a significant decrease in the cumulative pore volume are noted with extensive hydromagnesite growth. Higher temperature and pH conditions favour the formation of lamellar-shaped *versus* nest-like hydromagnesite. Factors such as SO_x and NO_x in industrial flue gas, as well as operation optimization, need further investigation for practical applications. These findings unlock the potential for harnessing these reactive CO_2 capture and mineralization for harnessing earth abundant magnesium hydroxide-rich tailings and anthropogenic CO_2 emissions to produce Mg-carbonate bearing end products for a sustainable energy and environmental future.

4 Experimental section

4.1 Chemicals

The reagents used in the study, magnesium hydroxide ($Mg(OH)_2$, 99%), sodium hydroxide (NaOH, 98%), and glycine (NH_2CH_2COOH, 99%) are procured from Sigma Aldrich. Na-glycinate solutions with concentrations of 1 M and 2.5 M are prepared by adding calculated amounts of sodium hydroxide and glycine to deionized water (18.2 MΩ cm, Millipore) while stirring at 300 rpm for 1 hour at room temperature. The formation of Na-glycinate can be expressed by the following chemical equation (reaction 1):

$$NH_2CH_2COOH + NaOH \leftrightarrow NH_2CH_2COO^- + Na^+ + H_2O \quad (1)$$

4.2 Experimental approach

4.2.1 Reactive CO_2 capture and mineralization with high purity CO_2. To investigate the influence of temperature and solvent concentration, experiments are conducted in a batch mode in which a slurry bearing $Mg(OH)_2$ and solvent such as

© 2025 The Author(s). Co-published by the Institute of Process Engineering, Chinese Academy of Sciences and the Royal Society of Chemistry

Ind. Chem. Mater., 2025, **3**, 732–743 | **739**

water or sodium glycinate is reacted with CO_2 (Fig. 9(a)). The slurry comprises 3 g of $Mg(OH)_2$ and 17 mL of water or the solvent, resulting in a weight ratio of 3 : 17 or 15 wt%. CO_2 gas (99.9% purity, Airgas Co., USA) is continuously injected into the reactor for five minutes to purge the residual air from the headspace. After the reactor is filled with CO_2, the outlet valve is slowly closed until the internal CO_2 pressure of 1 atm is reached. Next, the reactions are initiated by turning on stirrer with a set point of 300 rpm and applying a set of temperatures: 25 °C, 50 °C, 75 °C, and 90 °C, respectively. The reaction duration is set to 3 hours for each temperature. At the end of the reaction, the reactor is cooled and the solid carbonate-bearing products are collected by vacuum filtration, washed with deionized water, and dried at 80 °C for 24 hours. All experiments were replicated three times to calculate error bars.

4.2.2 Reactive CO_2 capture and mineralization using binary mixtures of CO_2 and N_2. Mixtures of CO_2 and N_2 gases with varying compositions of 4, 10, 15, and 20 vol% are prepared to investigate the influence of CO_2 compositions representative of industrial flue gas streams on reactive CO_2 capture and mineralization of $Mg(OH)_2$. As shown in Fig. 9(b), a pipe system with gas mixer and flow meter is developed to vary CO_2 concentrations for simulating exhaust flue gas. This gas mixture is injected into the beaker *via* a gas diffuser at a constant flow rate of 100 SCCM for 6 hours.

To investigate the influence of pre-loaded CO_2 capture solvents on reactive CO_2 capture and mineralization behaviour with $Mg(OH)_2$, experiments are conducted for 3 hours in the presence of various CO_2 and N_2 mixtures. The hypothesis that the initial loading of CO_2 overcomes the challenge of limited CO_2 availability initially and enables faster kinetics of carbon mineralization, is investigated. The ratio of $Mg(OH)_2$ to the solvent is 3 : 17 resulting in 15 wt% of solids in the system. The slurry is well-stirred at 300 rpm. The solid products are recovered through vacuum filtration, washed in deionized water, and dried at 80 °C for 48 hours before further characterization. All experiments were replicated three times to calculate error bars.

4.3 Determination of the extent of carbon mineralization

The extent of carbon mineralization defines CO_2 mineralization conversion of $Mg(OH)_2$ with respect to the theoretical maximum. In other words, this extent refers to the mole fraction of $Mg(OH)_2$ that converts into solid carbonate after mineralization. In this study, hydromagnesite ($Mg_5[(CO_3)_4(OH)_2]\cdot4H_2O$), a hydrated form of magnesium carbonate is formed and is the only product of carbon mineralization, as determined by X-ray diffraction (XRD) and thermo-gravimetric analyses (TGA).[51] The formation of hydromagnesite *via* carbon mineralization is shown in reaction 2.[21] Accordingly, the extent of carbon mineralization can be defined as the ratio between the captured mole of CO_2 and the theoretical CO_2 mole capacity of the sorbent.[52]

$$5Mg(OH)_2 + 4CO_2 = Mg_5[(CO_3)_4(OH)_2]\cdot4H_2O \qquad (2)$$

$$EoC = \frac{Wt\%_M/M_M}{Wt\%_M/M_M + (1-Wt\%_M)/M_B} \times 100\% \qquad (3)$$

In the expression above, EoC refers to the extent of carbon mineralization, $Wt\%_M$ refers to the weight percent of magnesium carbonate in the fully dried samples, while the M_M and M_B refer to the molecular weight of magnesium carbonate and brucite or magnesium hydroxide, respectively. Here, thermogravimetric analysis (TGA) is used to determine $Wt\%_M$. As shown in eqn (4), TGA is the actual weight loss of the fully dried samples in the temperature range 300–600 °C, while TGA_M and TGA_B refer to the theoretical weight loss of pure magnesium carbonate and magnesium hydroxide, respectively. Magnesium carbonate ($MgCO_3 \rightarrow MgO + CO_2$) and magnesium hydroxide ($Mg(OH)_2 \rightarrow MgO + H_2O$) decompose at 300–600 °C, the TGA_M and TGA_B values are calculated to be 52.20% and 30.89%, respectively.

$$Wt\%_M = \frac{TGA - TGA_B}{TGA_M - TGA_B} \times 100\% \qquad (4)$$

4.4 Characterization of the carbonate – bearing products

The chemical compositions and the morphological features of the carbonate-bearing products are analysed to provide insights into the mechanisms of reactive CO_2 capture and mineralization. The CO_2 content in the carbonate-bearing products is determined using thermogravimetric analysis (TGA, TA Instruments, SDT 650), in which the temperature is
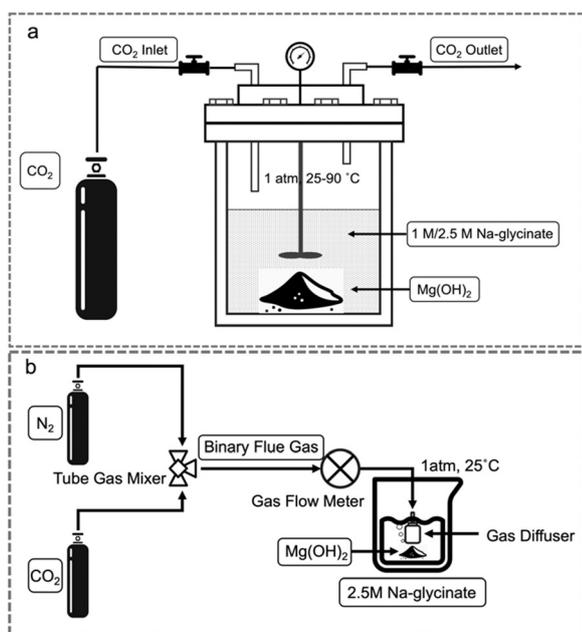

Fig. 9 Schematic representation of the integrated CO_2 capture and mineralization with (a) pure CO_2 and (b) mixed gases composed of CO_2 and N_2.

ramped from 25 °C to 1000 °C with a 2 °C min^{-1} ramping rate. Temperatures in the range of 300–500 °C are of particular interest since CO_2 and water releases occur in this range. The magnesium carbonate phases present are determined using wide-angle X-ray scattering (WAXS) measurements. These measurements are conducted at Sector 9-ID-C at the Advanced Photon Source (APS) in Argonne National Laboratory (ANL). For these experiments, the X-ray energy is set to 21.0 keV, which corresponds to the wavelength of 0.59 Å. The total X-ray flux during the measurements is 10^{13} photons mm^{-2} s^{-1}.[53] Detailed information about the instrument is reported in prior publications.[54,55] To further confirm the chemical bonds and functional groups in the carbonate-bearing products, attenuated total reflectance Fourier transform-infrared spectroscopy (ATR-FTIR, Nicolet FT-IR IS50, Thermo Scientific) analyses are performed. The morphological features and the particle size distributions are analysed using field emission scanning electron microscope (FESEM, LEO 1550 FESEM, Bruker) and the laser diffraction particle size analyzer (PSA, Anton Paar), respectively. The surface area and pore size distributions (PSD) before and after carbon mineralization are determined from N_2 adsorption–desorption isotherms using the Brunauer–Emmett–Teller (BET) method and Barrett–Joyner–Halenda (BJH) method, respectively (Quantachrome Autosorb iQ Analyzer, Boynton Beach, FL). Prior to measuring the adsorption–desorption isotherms, the samples were outgassed at 120 °C for 18 hours.

Data availability

The data supporting this article have been included in the main manuscript and as part of the ESI.†

Author contributions

Greeshma Gadikota – supervision, conceptualization, data curation, formal analysis, funding acquisition, investigation, methodology, project administration, resources, software, validation, visualization, writing – original draft, writing – review & editing. Xun Gao – investigation, data curation, formal analysis, methodology, resources, software, validation, visualization, writing – original draft, writing – review & editing. Peilong Lu – validation, visualization, writing – review & editing. Ivan Kuzmenko – investigation. Jan Ilavsky – investigation.

Conflicts of interest

Greeshma Gadikota is the co-founder of Carbon To Stone which is commercializing technologies for industrial decarbonization and carbon management. The other authors declare that they have no known competing financial interests or personal relationships that could have appeared to influence the work reported in this paper.

Acknowledgements

References

1 A. L. Harrison, I. M. Power and G. M. Dipple, Accelerated carbonation of brucite in mine tailings for carbon sequestration, *Environ. Sci. Technol.*, 2013, **47**, 126–134.

2 A. L. Harrison, G. M. Dipple, I. M. Power and K. U. Mayer, Influence of surface passivation and water content on mineral reactions in unsaturated porous media: Implications for brucite carbonation and CO_2 sequestration, *Geochim. Cosmochim. Acta*, 2015, **148**, 477–495.

3 I. M. Power, A. L. Harrison and G. M. Dipple, Accelerating mineral carbonation using carbonic anhydrase, *Environ. Sci. Technol.*, 2016, **50**, 2610–2618.

4 K. Rausis, A. Ćwik and I. Casanova, Phase evolution during accelerated CO_2 mineralization of brucite under concentrated CO_2 and simulated flue gas conditions, *J. CO2 Util.*, 2020, **37**, 122–133.

5 E. S. Sanz-Pérez, C. R. Murdock, S. A. Didas and C. W. Jones, Direct capture of CO_2 from ambient air, *Chem. Rev.*, 2016, **116**, 11840–11876.

6 X. Wang and C. Song, Carbon capture from flue gas and the atmosphere: A perspective, *Front. Energy Res.*, 2020, **8**, 560849.

7 A. Sanna, M. Uibu, G. Caramanna, R. Kuusik and M. M. Maroto-Valer, A review of mineral carbonation technologies to sequester CO_2, *Chem. Soc. Rev.*, 2014, **43**, 8049–8080.

8 P. Ochonma, X. Gao and G. Gadikota, Tuning reactive crystallization pathways for integrated CO_2 capture, conversion, and storage via mineralization, *Acc. Chem. Res.*, 2024, **57**, 267–274.

9 T. Yin, S. Yin, A. Srivastava and G. Gadikota, Regenerable solvents mediate accelerated low-temperature CO_2 capture and carbon mineralization of ash and nano-scale calcium carbonate formation, *Resour., Conserv. Recycl.*, 2022, **180**, 106209.

10 M. Liu, A. Hohenshil and G. Gadikota, Integrated CO_2 capture and removal via carbon mineralization with inherent regeneration of aqueous solvents, *Energy Fuels*, 2021, **35**, 8051–8068.

© 2025 The Author(s). Co-published by the Institute of Process Engineering, Chinese Academy of Sciences and the Royal Society of Chemistry

Ind. Chem. Mater., 2025, **3**, 732–743 | 741

11 X. Liu, S. Zhang, Q.-W. Song, X.-F. Liu, R. Ma and L.-N. He, Cooperative calcium-based catalysis with 1,8-diazabicyclo[5.4.0]-undec-7-ene for the cycloaddition of epoxides with CO_2 at atmospheric pressure, *Green Chem.*, 2016, **18**, 2871–2876.

12 J. M. Kang, *et al.*, Energy-efficient chemical regeneration of AMP using calcium hydroxide for operating carbon dioxide capture process, *Chem. Eng. J.*, 2018, **335**, 338–344.

13 P. C. Chen and S.-Z. Lin, Optimization in the absorption and desorption of CO_2 using sodium glycinate solution, *Appl. Sci.*, 2018, **8**, 2041.

14 F. M. Brethomé, N. J. Williams, C. A. Seipp, M. K. Kidder and R. Custelcean, Direct air capture of CO_2 via aqueous-phase absorption and crystalline-phase release using concentrated solar power, *Nat. Energy*, 2018, **3**, 553–559.

15 M. Liu, H. Asgar, S. Seifert and G. Gadikota, Novel aqueous amine looping approach for the direct capture, conversion, and storage of CO_2 to produce magnesium carbonate, *Sustainable Energy Fuels*, 2020, **4**, 1265–1275.

16 L. Zhao, L. Sang, C. Jun, J. Ji and H. H. Teng, Aqueous carbonation of natural brucite: Relevance to CO_2 sequestration, *Environ. Sci. Technol.*, 2010, **44**, 406–411.

17 T. Dudev and C. Lim, Importance of metal hydration on the selectivity of Mg^{2+} versus Ca^{2+} in magnesium ion channels, *J. Am. Chem. Soc.*, 2013, **135**, 17200–17208.

18 M. Liu and G. Gadikota, Single-step, low-temperature and integrated CO_2 capture and conversion using sodium glycinate to produce calcium carbonate, *Fuel*, 2020, **275**, 117887.

19 P. Bénézeth, G. D. Saldi, J.-L. Dandurand and J. Schott, Experimental determination of the solubility product of magnesite at 50 to 200°C, *Chem. Geol.*, 2011, **286**, 21–31.

20 D. Guo, *et al.*, Amino acids as carbon capture solvents: Chemical kinetics and mechanism of the glycine + CO_2 reaction, *Energy Fuels*, 2013, **27**, 3898–3904.

21 Q. Gautier, P. Bénézeth, V. Mavromatis and J. Schott, Hydromagnesite solubility product and growth kinetics in aqueous solution from 25 to 75°C, *Geochim. Cosmochim. Acta*, 2014, **138**, 1–20.

22 S. M. Klara, CO_2 solubility in water and brine under reservoir conditions, *Chem. Eng. Commun.*, 1990, **90**, 23–33.

23 P. Birkle and I. S. Torres-Alvarado, *Water-Rock Interaction*, CRC Press, 2010.

24 D. Daval, R. Hellmann, G. D. Saldi, R. Wirth and K. G. Knauss, Linking nm-scale measurements of the anisotropy of silicate surface reactivity to macroscopic dissolution rate laws: New insights based on diopside, *Geochim. Cosmochim. Acta*, 2013, **107**, 121–134.

25 X. Gao, D. Prasad, M. A. Mahadik and G. Gadikota, Enhanced H_2 recovery by coupling the water-gas shift reaction with in-situ CO_2 capture and mineralization using earth-abundant Ca- and Mg-silicates and hydroxides, *React. Chem. Eng.*, 2025, DOI: **10.1039/D4RE00480A**.

26 C. Blaquiere and G. Berthon, Speciation studies in relation to magnesium bioavailability: Formation of Mg(II) complexes with glutamate, aspartate, glycinate, lactate, pyroglutamate, pyridoxine, and citrate, and appraisal of their potential significance towards magnesium gastrointestinal absorption, *Inorg. Chim. Acta*, 1987, **135**, 179–189.

27 R. Weber, S. Orsino, N. Lallemant and A. Verlaan, Combustion of natural gas with high-temperature air and large quantities of flue gas, *Proc. Combust. Inst.*, 2000, **28**, 1315–1321.

28 F. Gholami, M. Tomas, Z. Gholami and M. Vakili, Technologies for the nitrogen oxides reduction from flue gas: A review, *Sci. Total Environ.*, 2020, **714**, 136712.

29 V. Majer, J. Sedlbauer and G. Bergin, Henry's law constant and related coefficients for aqueous hydrocarbons, CO_2 and H_2S over a wide range of temperature and pressure, *Fluid Phase Equilib.*, 2008, **272**, 65–74.

30 A. Botha and C. A. Strydom, DTA and FT-IR analysis of the rehydration of basic magnesium carbonate, *J. Therm. Anal. Calorim.*, 2003, **71**, 987–996.

31 C. M. Janet, B. Viswanathan, R. P. Viswanath and T. K. Varadarajan, Characterization and photoluminescence properties of MgO microtubes synthesized from hydromagnesite flowers, *J. Phys. Chem. C*, 2007, **111**, 10267–10272.

32 T. Selvamani, A. Sinhamahapatra, D. Bhattacharjya and I. Mukhopadhyay, Rectangular MgO microsheets with strong catalytic activity, *Mater. Chem. Phys.*, 2011, **129**, 853–861.

33 R. Černý, V. Valvoda and M. Chládek, Empirical texture corrections for asymmetric diffraction and inclined textures, *J. Appl. Crystallogr.*, 1995, **28**, 247–253.

34 M. Akao and S. Iwai, The hydrogen bonding of hydromagnesite, *Acta Crystallogr., Sect. B*, 1977, **33**, 1273–1275.

35 A. Abu Fara, M. R. Rayson, G. F. Brent, T. K. Oliver, M. Stockenhuber and E. M. Kennedy, Formation of magnesite and hydromagnesite from direct aqueous carbonation of thermally activated lizardite, *Environ. Prog. Sustainable Energy*, 2019, **38**(3), e13244.

36 Y. Wang, *et al.*, Preparation, properties and phase transition of mesoporous hydromagnesite with various morphologies from natural magnesite, *Powder Technol.*, 2020, **364**, 822–830.

37 H. Pang, G. Ning, W. Gong, J. Ye and Y. Lin, Direct synthesis of hexagonal $Mg(OH)_2$ nanoplates from natural brucite without dissolution procedure, *Chem. Commun.*, 2011, **47**, 6317–6319.

38 D. Bhattacharjya, T. Selvamani and I. Mukhopadhyay, Thermal decomposition of hydromagnesite: Effect of morphology on the kinetic parameters, *J. Therm. Anal. Calorim.*, 2012, **107**, 439–445.

39 T. Selvamani, T. Yagyu, S. Kawasaki and I. Mukhopadhyay, Easy and effective synthesis of micrometer-sized rectangular MgO sheets with very high catalytic activity, *Catal. Commun.*, 2010, **11**, 537–541.

40 S. Guermech, J. Mocellin, L.-H. Tran, G. Mercier and L.-C. Pasquier, A study of hydromagnesite and nesquehonite precipitation in indirect aqueous carbonation of thermally activated serpentine in a batch mode, *J. Cryst. Growth*, 2022, **584**, 126540.

41 H. Y. Atay and E. Çelik, Use of Turkish huntite/hydromagnesite mineral in plastic materials as a flame retardant, *Polym. Compos.*, 2010, **31**, 1692–1700.

42 A. A. Basfar and H. J. Bae, Influence of magnesium hydroxide and huntite hydromagnesite on mechanical properties of ethylene vinyl acetate compounds crosslinked by dicumyl peroxide and ionizing radiation, *J. Fire Sci.*, 2010, **28**, 161–180.

43 Q. Li, Y. Ding, G. Yu, C. Li, F. Li and Y. Qian, Fabrication of light-emitting porous hydromagnesite with rosette-like architecture, *Solid State Commun.*, 2003, **125**, 117–120.

44 D. A. Vermilyea, The dissolution of MgO and Mg(OH)$_2$ in aqueous solutions, *J. Electrochem. Soc.*, 1969, **116**, 1179.

45 R. Hay, N. T. Dung, A. Lesimple, C. Unluer and K. Celik, Mechanical and microstructural changes in reactive magnesium oxide cement-based concrete mixes subjected to high temperatures, *Cem. Concr. Compos.*, 2021, **118**, 103955.

46 S. Katre, P. Ochonma, H. Asgar, A. M. Nair, K. Ravi and G. Gadikota, Mechanistic insights into the co-recovery of nickel and iron via integrated carbon mineralization of serpentinized peridotite by harnessing organic ligands, *Phys. Chem. Chem. Phys.*, 2024, **26**, 9264–9283.

47 G. Gadikota, J. Matter, P. Kelemen and A. H. A. Park, Chemical and morphological changes during olivine carbonation for CO$_2$ storage in the presence of NaCl and NaHCO$_3$, *Phys. Chem. Chem. Phys.*, 2014, **16**, 4679–4693.

48 G. Gadikota, Carbon mineralization pathways for carbon capture, storage, and utilization, *Commun. Chem.*, 2021, **4**, 23.

49 G. Gadikota, Multiphase carbon mineralization for the reactive separation of CO$_2$ and directed synthesis of H$_2$, *Nat. Rev. Chem.*, 2020, **4**, 78–89.

50 M. Liu and G. Gadikota, Integrated CO$_2$ capture, conversion, and storage to produce calcium carbonate using an amine looping strategy, *Energy Fuels*, 2019, **33**, 1722–1733.

51 L. A. Hollingbery and T. R. Hull, The thermal decomposition of huntite and hydromagnesite—A review, *Thermochim. Acta*, 2010, **509**, 1–11.

52 A. A. Olajire, A review of mineral carbonation technology in sequestration of CO$_2$, *J. Pet. Sci. Eng.*, 2013, **109**, 364–392.

53 X. Gao, H. Asgar, I. Kuzmenko and G. Gadikota, Architected mesoporous crystalline magnesium silicates with ordered pore structures, *Microporous Mesoporous Mater.*, 2021, **327**, 111381.

54 J. Ilavsky, F. Zhang, A. J. Allen, L. E. Levine, P. R. Jemian and G. G. Long, Ultra-small-angle X-ray scattering instrument at the Advanced Photon Source: History, recent development, and current status, *Metall. Mater. Trans. A*, 2013, **44**, 68–76.

55 U. Bonse and M. Hart, Tailless X-ray single-crystal reflection curves obtained by multiple reflection, *Appl. Phys. Lett.*, 1965, **7**, 238–240.

© 2025 The Author(s). Co-published by the Institute of Process Engineering, Chinese Academy of Sciences and the Royal Society of Chemistry

Ind. Chem. Mater., 2025, **3**, 732–743 | **743**